Computational Imaging to Compensate for Soft-Tissue Deformations in Image-Guided Breast Conserving Surgery

Winona L. Richey, Jon S. Heiselman, Morgan J. Ringel, Ingrid. M. Meszoely, and Michael I. Miga*,
Member, IEEE

Abstract— Objective: **During breast conserving surgery (BCS), magnetic resonance (MR) images aligned to accurately display intraoperative lesion locations can offer improved understanding of tumor extent and position relative to breast anatomy. Unfortunately, even under consistent supine conditions, soft tissue deformation compromises image-to-physical alignment and results in positional errors.** *Methods:* **A finite element inverse modeling technique has been developed to nonrigidly register preoperative supine MR imaging data to the surgical scene for improved localization accuracy during surgery. Registration is driven using sparse data compatible with acquisition during BCS, including corresponding surface fiducials, sparse chest wall contours, and the intra-fiducial skin surface. Deformation predictions were evaluated at surface fiducial locations and subsurface tissue features that were expertly identified and tracked. Among *n*=7 different human subjects, an average of 22 ± 3 distributed subsurface targets were analyzed in each breast volume.** *Results:* **The average target registration error (TRE) decreased significantly when comparing rigid registration to this nonrigid approach (10.4 ± 2.3 mm vs 6.3 ± 1.4 mm TRE, respectively). When including a single subsurface feature as additional input data, the TRE significantly improved further (4.2 ± 1.0 mm TRE), and in a region of interest within 15 mm of a mock biopsy clip TRE was 3.9 ± 0.9 mm.** *Conclusion:* **These results demonstrate accurate breast deformation estimates based on sparse-data-driven model predictions.** *Significance:* **The data suggest that a computational imaging approach can account for image-to-surgery shape changes to enhance surgical guidance during BCS.**

Index Terms— **biomechanical models, breast conserving surgery, deformation, image-guided surgery, lumpectomy, registration**

I. INTRODUCTION

I N the United States, breast cancer is the most common cancer in women and will be diagnosed in an estimated 290,560 people this year [2]. The majority of these patients will be recommended for breast conserving surgery (BCS) [3, 4], a tissue-sparing procedure that consists of surgical removal of the lesion and a margin of healthy tissue surrounding that lesion. Unfortunately, the patient position in surgery is very different from the position for most diagnostic breast imaging, making imaging information underutilized in surgery. For diagnostic magnetic resonance (MR) imaging, a patient is lying prone, or face down, with the breast pendant within an imaging radiofrequency coil. For diagnostic ultrasound imaging, the patient lies supine, or face up, with the arm fully abducted beside the head. For mammography, the patient is standing with the breast compressed between two plates. None of these imaging positions are representative of surgical position. In surgery, a patient lies supine with the arm outstretched laterally at 90°, i.e. in a T-shape. As a result of this incongruence between diagnostic imaging and surgical presentation, it can be challenging for surgeons to relate the tumor location in a medical image volume to its intraoperative counterpart on the operating table. In addition, studies have emerged demonstrating that switching from prone to supine imaging presentations induces tumor shape and size differences, as well as a shift in the tumor position with respect to all available anatomical landmarks [5-7]. Even under ideal circumstances when a patient remains in a supine configuration during imaging, simple 90° abduction of the arm results in significant shifts and shape changes in breast tissue [8]. In fact, even simple intraprocedural changes such as small rotations of the operating room table can result in significant remaining alignment errors after rigid registration [8].

In an effort to overcome difficulties surrounding intraoperative lesion localization during BCS, several techniques have been established to provide positional information during surgery. Wire-guided localization involves inserting a guide wire into the center of a tumor using cross-sectional image guidance. In surgery, the surgeon uses the wire as a guide path to the region of interest. However, in radiology the guide wire placement technology is geometrically constrained and can lead to resection paths that are suboptimal. Additionally, as these wires are placed potentially hours before the surgery, the protruding wire can become displaced. Most importantly, even with optimal wire placement and successful resection along the wire path, the

surgeon must estimate the relative position of the wire tip within the lesion and must also approximate the exact tumor boundary surrounding the unseen wire tip when resecting a suitable surgical margin.

Though guide wire approaches are still in use, in the past decade, the expanding use of implanted seed-based markers (e.g. radioactive, magnetic, and radar reflector seeds) is beginning to replace guide wire approaches. For seed-based methods, a small localization marker is implanted near the lesion by radiology in the days or weeks before surgery. The placement of the marker is then confirmed with imaging. The seed is localized intraoperatively using a handheld probe that reports the seed-to-probe distance. Though these seed-based techniques offer improvement over wire guidance, reoperation rates remain high due to residual disease after resection, or positive margins. Average reoperation rates are reported up to 30%, with most averages around 10–20% [9-11]. These methods provide seed location and allow for unconstrained trajectory to a target, but they cannot provide guidance for boundary management during resection to excise the precise deformed lesion shape. In recent years, reoperation rates have plateaued around 10–20% [10, 12, 13], suggesting that these approaches may be at their resolution limit.

Intraoperative MR imaging can provide the shape of the tumor on the operating table, but requires the use of nonmagnetic tools and interruption of surgery for imaging [7]. Additionally, intraoperative MR is not widely available, as most operating rooms are not equipped with MR scanners. Alternatively, ultrasound can be used within the sterile field throughout the procedure to visualize echogenic tumors intraoperatively. The transducer can also be used to investigate the resection cavity for remaining tumor after the initial excision. One of the largest drawbacks to intraoperative ultrasound is that not all lesions are visible on ultrasound. Though intraoperative ultrasound provides low rates of positive margins (2–14%) [14-16], only 50% of non-palpable tumors are visible on ultrasound [17]. There remains a need for 3D guidance that can be used for a larger majority of patients.

Image guidance systems can provide information about full tumor boundaries by registering, or aligning, preoperative imaging with the physical patient space. For BCS, these research systems typically use preoperative MR imaging [18-20] as it offers high sensitivity [21, 22] and, when performed in a supine position, can provide an improved understanding of intraoperative tumor shape and position [6, 23, 24]. There are several ways supine MR data have been leveraged in the operating room. Sakakibara et al. positioned patients in a surgical pose for MR imaging and used a projector to display tumor extent directly onto the breast surface during surgery. This method produced smaller resection volumes and lower positive margin rates than wire guidance [25]. Recently, Wu et al. achieved 18% positive margin rates by tracing tumor positions onto the skin surface using a patient specific 3D printed breast mold derived from supine MR imaging [26]. These methods show the value of supine MR in determining intraoperative tumor extent. However, their reliance on a skin surface projection still provides limited understanding of tumor depth and makes them inadequate for complete 3D margin management during resection.

Image guidance systems that incorporate 3D renderings can show the full tumor extent based on preoperative imaging. An image guidance system from Pallone et al. expanded upon these skin surface projections by including a 3D model view and tracked tools [27]. When evaluated on 69 patients in a randomized controlled prospective study, their system showed a 9% positive margin rate under current margin guidelines, which was lower than for wire-guided BCS. Though this did not meet a level of statistical significance (p=0.08), it is certainly suggestive [19]. In separate work, Perkins et al. integrated MR imaging into an augmented reality system for BCS with promising qualitative validation [20].

Although the aforementioned approaches aim to display preoperative tumor extent registered to the intraoperative space, the reliance on rigid registration between image and physical spaces represents a substantial limitation. Though simple linear shifts are easily accommodated with rigid approaches, there is a considerable degree of nonrigid deformation that occurs between imaging positioning and surgical presentation, even for supine-to-supine registrations [8]. Abduction of the arm, re-positioning of the patient, and rotation of the operating table all contribute to discrepancies between imaging and surgical tumor location. Due to these nonrigid shifts, residual error after rigid registration can be large—on the order of 10–30 mm on the surface [8]. Localization inaccuracies can lead to larger resected specimen volumes, positive margins, or both. In fact, in qualitative evaluation, [20] notes the conspicuous need for nonrigid correction due to obvious misalignments after rigid registration.

Nonrigid deformation correction for breast cancer surgery has been limitedly explored, especially within the context of the clinically relevant supine-to-supine registration problem. However, initial findings suggest that nonrigid registration approaches can improve accuracy for BCS. Ebrahimi et al. observed deformations from full abduction of the arm in supine MR images, and used thin plate splines on 24–34 fiducials well distributed across the breast surface to correct for deformations. Though the method had no biophysical link, accuracy at tumor centroids in six patients improved from 3–18 mm with rigid registration to 1–10 mm. However, improvement across all cases was variable [28]. Although the approach performed very well for some cases, in one case error actually increased with nonrigid registration.

Conley et al. introduced a nonrigid correction method that employed a forward solved finite element method (FEM) using sparse data collection in a mock-intraoperative setting [18]. Following preoperative supine MR imaging, mock-intraoperative data were collected including surface fiducial locations marked with tracked tools, surface collection with a laser range scanner, and the chest wall position measured with tracked ultrasound. An initial image-to-physical rigid registration was performed, and the remaining fiducial mismatch was used to estimate surface displacements. A

patient specific breast mesh was assumed to experience loading in the craniocaudal direction only at inferior and superior mesh boundaries. This work reduced two tumor centroid errors from 6.5 and 12.5 mm with rigid registration to 5.5 and 5.3 mm after correction, respectively [18]. Although the nonrigid approach offered improvement, the number of cases was limited and the value of the method was inconsistent, offering 15% and 58% improvement in the two cases evaluated. While the work was interesting, unfortunately, the assumption of only craniocaudal boundary forces from observed surface fiducial movements is likely a limitation. The approach did not account for displacements in the medial-lateral, and anterior-posterior directions which collectively are approximately equal to the craniocaudal displacements according to a recent study by Richey *et. al.* [8].

In the work presented here, an inverse modeling approach is employed to predict breast deformation from abduction of the arm. In contrast to forward models, inverse modeling approaches can be designed to reconstruct forces at the anatomical locations that experience true mechanical loading. Here, the linearized iterative boundary reconstruction (LIBR) method, as presented in [29], has been modified for clinical application in BCS. The LIBR method solves for a distributed profile of applied mechanical loading that produces the observed intraoperative breast shape change given a set of sparse data constraints. Once the shape change has been reconstructed, a navigation system can be updated with a deformed image volume that constitutes a computational image of the new tissue state. Another important contribution of this work is the degree of validation that is offered in the evaluation. Previous work in nonrigid breast registration has been very limited. Here, the modified LIBR approach is evaluated on 157 subsurface targets well distributed within the breast volumes of n=7 human subjects, thus providing a global volumetric evaluation of target registration errors.

II. METHODS

A. Overview of Experimental Protocol

A mock operating room (OR) experiment was conducted on n=7 healthy volunteers. Supine MR imaging provided a mock-preoperative scan with the arm at the subject's side. Repeat imaging was conducted with the subject in an alternate configuration with the ipsilateral arm fully abducted. The supine MR with fully abducted arm was treated as a mock-intraoperative configuration, from which sparse data were extracted to represent an extent feasible for intraoperative collection. This extent is representative of acquisition in physical surgical space that would remain minimally disruptive to surgical workflow. With data obtained in the mock-preoperative and the mock-intraoperative states, a novel image-to-physical registration approach was performed and evaluated. Accuracy assessment involved transforming novel (not used as part of the registration) subsurface targets from the mock-preoperative location to their predicted mock-intraoperative location and then comparing to the manually measured counterpart in the acquired mock-intraoperative

state. The evaluation involved on average 22 ± 3 subsurface targets across the data set, comprising a total number of 157 corresponding target points. Lastly, as patients generally have biopsy clips and/or a localization marker implanted in the breast prior to surgery, the evaluation experiment was extended to include the impact on alignment if a single subsurface feature could also be incorporated into the sparse set of intraoperatively acquired data.

B. Human Imaging.

Data were collected on seven healthy volunteers as approved by the Institutional Review Board at Vanderbilt University (protocol code 130038, date of approval 11/11/2015). Volunteers ranged from 23 to 57 years of age (average age of 29 ± 12) with breast volumes of 398 to 1228 cm^3 (average volume of 688 ± 256 cm^3). As noted above, the mock-preoperative imaging state involves supine imaging with the arms down within the closed MR bore. As discussed, surgical positioning involves the arm abducted 90° in a T-shape orientation and previous work supports significant shape change between these two states [8]. This configuration is not possible within the scanner. Here, to provide full volumetric MR data for comprehensive subsurface validation, the fully abducted position was used to approximate the surgical position. It should be noted that this represents a more considerable challenge than the T-shape surgical presentation. In previous work, the shape change for the fully abducted arm is approximately 45% larger in magnitude than the halfway abducted surgical presentation [8].

With respect to specific protocol, two supine MR images were obtained sequentially: one with the arm down beside the torso, and a second with the arm up beside the head. In both scans, the contralateral arm was down. Before scanning, 26 fiducials (IZI Medical Products, Owing Mills, MD) were evenly distributed across the breast surface. These fiducials are visible in both MR images and serve as corresponding surface points. Due to the significant breast shifts, after abduction some fiducials moved to outside the image field of view; at least 23 corresponding fiducials were recognized in each case. Images were obtained on closed bore 3T Phillips scanners using a 16-channel torso coil with padded support to reduce compression of the breasts. In one case a plastic cage was placed around the subject's torso to fully suspend the coil, eliminating tissue compression. It should be noted that the plastic cage wholly eliminated breast compression (similar to proper application of padded coil support) with the added benefit of simplifying subject repositioning. A THRIVE sequence was used with one of two voxel resolutions, 0.357×0.357×1 mm^3, or 0.391×0.391×1 mm^3 voxel size. The THRIVE pulse sequence does not compensate for respiratory and cardiac motions. However, motion artifacts were not noticeable for the majority of volunteers in this study. Though one subject had noticeable respiratory artifact, this artifact was small enough that image features were still able to be selected with no change to the imaging procedure (e.g. respiratory gating).
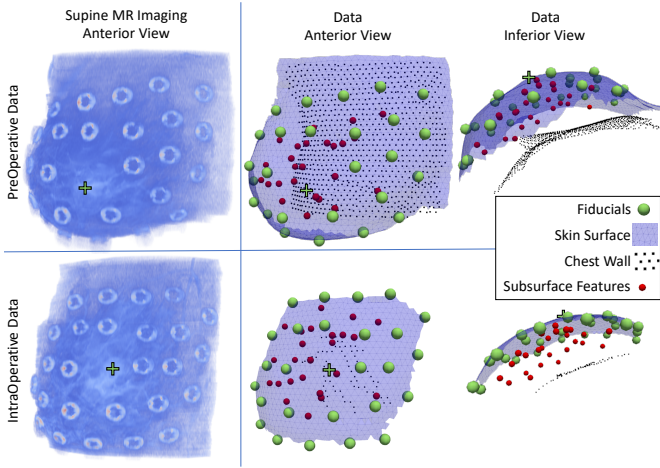
Fig. 1. Exemplar data for one subject, rendered in ParaView [1]. Supine MR projection images (left) with nipple displayed as +, and extracted data (right). The model is evaluated at the subsurface features (red), which were not used to drive the correction.

C. Image Derived Data

The breast volumes of both the mock preoperative and intraoperative breast state were segmented manually to include the skin, ligaments and adipose tissues. Chest wall was not included in the breast tissue segmentation. To improve the speed of segmentation, automatic interpolation in ITK-SNAP [30] was used, segmenting every 5-10 slices in the axial direction. Generally, an experienced user takes 15-30 minutes to segment the breast depending on complexity of the breast shape. Custom mesh generation software was used to generate patient specific 3D meshes from the breast segmentations of both states [31]. Meshes were discretized to tetrahedral elements with 4 mm edge length. Mock-preoperative breast meshes ranged from approximately 6,500–18,000 vertices.

The supine MR images provided the following data as shown in Figure 1: (1) corresponding locations of the MR-visible synthetic surface fiducials, (2) the breast skin surface, (3) the chest wall, and (4) subsurface feature locations used for validation. All features were designated manually, and all surfaces were subsampled from the boundary of the patient specific 3D mesh. To simulate realistic intraoperative data collection, a sparse data set was taken from the mock-intraoperative state (arm-abducted MR image). For the mock-intraoperative state, the sparse chest wall data included a set of chest wall contours simulating collection from 7–10 linear probe ultrasound images with 40 mm width. It should be noted that the distribution of chest wall sample contours was based on previous work in a tracked ultrasound study measuring the chest wall in a mock-intraoperative setting using a BK5000 18L5 linear probe (BK Medical UK Ltd., Peabody, MA) [8]. Contours were designated manually, each contour taking only a few seconds to segment. With respect to the breast skin surface, intraoperative segmentations were subsampled from the breast mesh boundary nodes to only include intrafiducial surface points. This process ensures that the extent of the intraoperative skin surface is entirely contained on the preoperative mesh. Lastly, the subsurface features used for validation were selected manually, choosing an average of

22 ± 3 (ranging from 18–26 across the data) well distributed homologous points for each subject. Throughout the seven breast volumes, a total of 157 corresponding points were identified.

D. Nonrigid Deformation Correction

This work employs the linearized iterative boundary reconstruction (LIBR) method, recently presented by Heiselman et al. [29], modified for breast-specific data. Here, breast deformations are assumed to be isotropic, homogeneous, and linearly elastic. The method supposes that tissue deforms according to the Navier Cauchy equations, which govern linear elasticity at static equilibrium [32]. Here, the Galerkin method of weighted residuals [33] using conventional linear local Lagrange polynomial interpolants with tetrahedra is used to determine approximate displacements which come close to the unknown true displacement field.

Briefly, the LIBR method solves for a set of boundary condition displacements that produce the observed intraoperative deformation state. A series of control points on the model surface are perturbed in each of the three Cartesian directions. Perturbations are in the form of displacement boundary conditions, i.e. Dirichlet conditions, and the resulting deformation solution is computed using the finite element method. Each point loading is relaxed to establish an equivalent distributed load with identical far-field behavior as the point source. The relaxed displacements resulting from each control point perturbation embody independent modes that characterize local responses to forces applied to the tissue. These deformation solutions can be linearly combined to iteratively reconstruct intraoperative organ deformations based on optimizing the objective function from [29],

$$\Omega(\boldsymbol{\alpha}, \boldsymbol{\tau}, \boldsymbol{\theta}) = \sum_F \frac{\omega_F}{N_F} \sum_{i=1}^{N_F} f_i^2 + \omega_E f_E^2 \qquad (1)$$

where f_i represents the distance between the position of an intraoperative data point provided to the correction algorithm and its counterpart on the registered preoperative model, f_E represents the strain energy of the deformation, ω_F represents the weight of a feature F, N_F represents the number of points within feature F, and ω_E represents the strain energy weight. The objective function is parameterized over a weight vector $\boldsymbol{\alpha}$ that encodes the deformation state, and rigid transformation parameters $\boldsymbol{\tau}$ and $\boldsymbol{\theta}$, which represent rigid translations and rigid rotations of the deforming model, respectively. Levenberg-Marquardt optimization is used, terminating when the step-wise error tolerance $\Delta\Omega < 10^{-12}$ is satisfied. Material parameters in the Navier Cauchy equations are set as in [29], with Young's Modulus $E = 2100$ Pa and Poisson's ratio, $v = 0.45$.

The LIBR method reported in [29] is modified to reflect the breast localization data described above, and (1) becomes
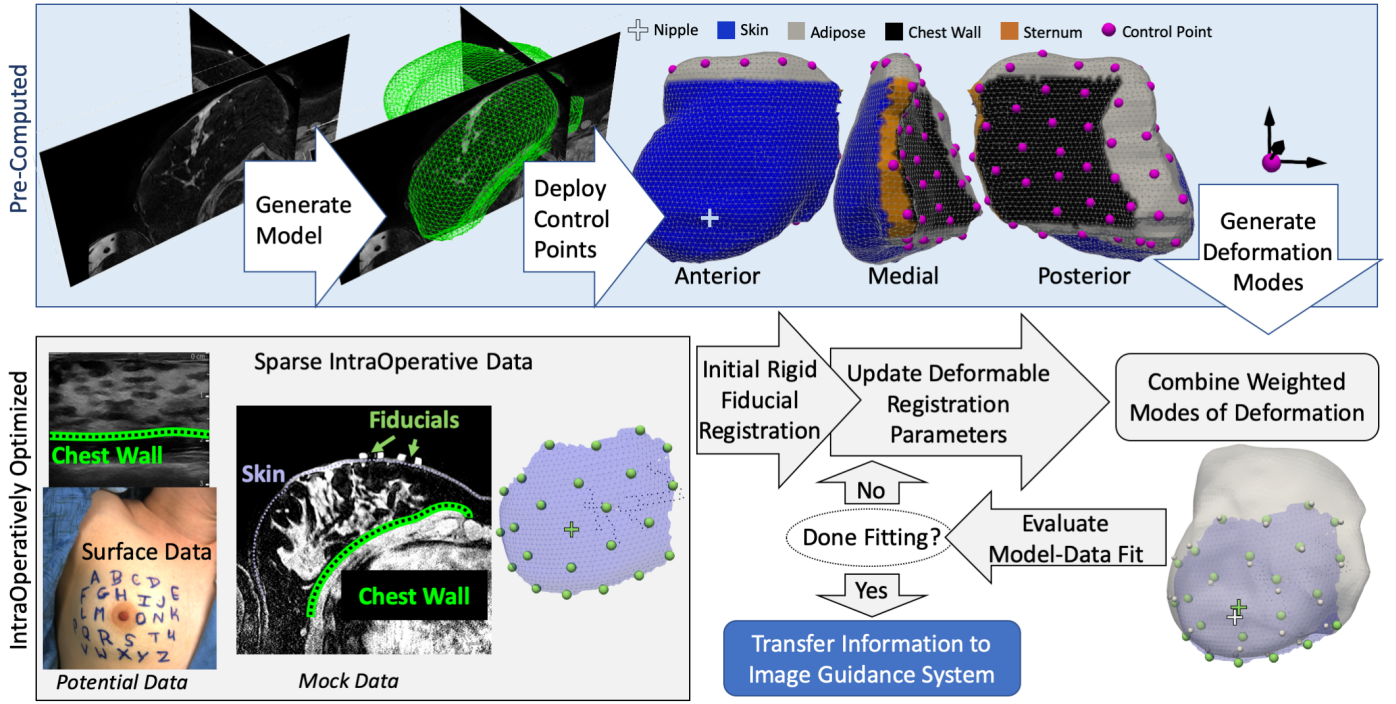
Fig. 2. Schematic of the method workflow, with precomputed steps (top) and intraoperative optimization steps (bottom). The nipple is consistently marked +.

$$\Omega(\boldsymbol{\alpha}, \boldsymbol{\tau}, \boldsymbol{\theta}) = \frac{1}{N_{fids}} \sum_{i=1}^{N_{fids}} f_i^2 + \frac{1}{N_{skin}} \sum_{i=1}^{N_{skin}} f_i^2$$
$$+ \frac{1}{N_{chest}} \sum_{i=1}^{N_{chest}} f_i^2 + \omega_E f_E^2 \qquad (2)$$

with the assumption that each data component of the objective function equally impacts its evaluation (i.e. ω_F=1.0 m^{-2}). The model-data misfit error, f_i, for each feature is computed based on the type of correspondence, with MR-visible fiducials (abbreviated as *fids*) treated as corresponding points, and skin and chest wall data treated as point-to-surface correspondences (or sliding constraints) as described in [29]. The strain energy weighting factor, ω_E, has been empirically determined and is fixed at 10^{-9} Pa^{-2}. The modeling workflow is summarized in Figure 2.

Control points serve as the action points of applied perturbations, and consist of 45 discrete locations dispersed across all the boundaries of the mesh, except for the skin surface. As in Heiselman *et al.*, k-means clustering was used to evenly distribute control points across the control surfaces [29]. The distribution of 45 control points, in magenta, on a preoperative breast mesh is shown in the top right of Figure 2 in anterior, medial, and posterior views. Tissue types are designated with skin in blue, sternum in orange, and chest wall in black. Internal tissue that is transected by the mesh is marked in grey. This control point distribution represents the boundary of the computational domain where mechanical displacements are applied with remaining areas assumed stress-free. Applied displacements ideally capture the forces internal to the subject's body but external to the meshed computational domain, i.e. forces exerted by ligaments or tension on tissue adjacent to the meshed domain. It should also be noted that in some cases the breast surface did come into contact with the MR torso coil. However, these forces were minimized with the weight of the coil supported by padding or a plastic cage. Therefore, this contact was considered to have negligible influence on the registration.

Throughout this work, surface fiducial registration error (FRE) and subsurface target registration error (TRE) are computed as the arithmetic mean and standard deviation of Euclidean distances between predicted data positions and the ground truth positions as measured in the mock-intraoperative MR.

E. Impact from Including a Single Nearest Neighbor Subsurface Feature

Clinically, it is quite possible to localize a subsurface point near the lesion intraoperatively. For example, before surgery, patients routinely have biopsy clips and/or localization markers implanted in the breast in close proximity of the tumor. These subsurface features serve to assist in localization during tissue resection and can be localized either with tracked ultrasound images or with other intraoperative localization approaches. On the former, approaches to account for deformations induced by ultrasound probe compression have been developed to enable accurate localization of subsurface targets with ultrasound [34]. With respect to the latter, investigators have developed custom seeds capable of being wirelessly tracked in 3D space during breast surgery [35, 36].

Given the common availability of a subsurface target near the region of interest, the impact of including a single subsurface feature on the LIBR approach was evaluated. For a given target, the nearest neighbor ($k=1$) subsurface feature was considered another tracked point and included as an additional input to the model. Thus $k=0$ indicates that no corresponding subsurface points were used. To accommodate, when $k=1$ the objective function (2) is modified to include this additional feature,

$$\Omega(\boldsymbol{\alpha},\boldsymbol{\tau},\boldsymbol{\theta}) = f_{feature}{}^2 + \frac{1}{N_{fids}}\sum_{i=1}^{N_{fids}} f_i{}^2 + \frac{1}{N_{skin}}\sum_{i=1}^{N_{skin}} f_i{}^2$$
$$+ \frac{1}{N_{chest}}\sum_{i=1}^{N_{chest}} f_i{}^2 + \omega_E f_E{}^2, \tag{3}$$

where $f_{feature}$ is the model-data fit at one subsurface feature point, treated as a corresponding point as outlined in [29].

Here, the additional feature is the target's nearest neighbor, i.e. the subsurface point closest to the evaluation target of interest. The average distance from a target to its nearest neighbor was 15.0 ± 6.6 mm. One subsurface feature was considered a target and a model optimization was performed. The model optimization included the data outlined in (3), where $f_{feature}$ is the model-data fit at the single target's nearest neighbor. Model accuracy was evaluated at the target of interest and across all surface fiducials. This process was then repeated, iterating through each target in the complete list of subsurface features.

Throughout this study, the subsurface TRE was only ever evaluated at novel points, i.e. it is never evaluated at any subsurface points used to drive the optimization. However, surface FRE is reported separately as residual error at surface fiducials that were used to drive the optimization.

F. Accuracy in Regions of Interest

Approximately 50% of breast lesions have radii smaller than 5 mm, and 77–87% have radii under 10 mm [37, 38]. Therefore, if planning to resect 10 mm of healthy tissue surrounding a lesion, as suggested in [6, 25, 39], over 50% of lesions would have planned resection volumes within an r=15 mm region of interest (ROI), and over 75% of lesions would fall well within an r=30 mm ROI. This means that the localization accuracy in these smaller regions of interest are clinically important.

As subsurface features in this work were selected to offer full coverage of the breast volume, distances between subsurface features are generally larger than the expected distance from a lesion to its implanted biopsy clip or localization seed. Conventional standard of care considers localization markers to be accurately placed when they are within 10 mm of a lesion, but here the average distance between a target and its driving nearest neighbor was 15.0 ± 6.6 mm. To extend the analysis, each subsurface feature was treated as a mock biopsy clip that was localized in the operating room (hereafter referred to as a clip). The model's predictive accuracy was then evaluated by considering all targets within a region of interest (ROI) surrounding each clip. While the nearest neighbor analysis in the previous subsection provides an evaluation framework at every subsurface point, the ROI analysis provides analysis only locally in the immediate tissue neighborhood near a clip of interest.

Radii were selected based on breast lesion sizes, offering localization accuracy within the ranges of realistic excision volumes (accounting for over 50% and 75% of patients for r=15 mm and r=30 mm respectively). A region of interest was defined centered around each clip using radii of r=15 mm, r=30 mm, and r=∞ mm. While this section focuses on local accuracy, it should be noted that a radius of r=∞ gives the full field improvement across the entire breast volume from the inclusion of one subsurface mock biopsy clip. As noted above, smaller radii describe accuracy in a local region of interest surrounding a mock biopsy clip.

The model-based registration approach was then implemented using breast surface and chest wall data in addition to the single subsurface mock clip as the driving spatial information. The objective function for this analysis still utilizes (3). Here, the additional feature is the subsurface clip of interest, and $f_{feature}$ is the model-data fit at that clip. The model evaluation differs with r, as all target errors within the ROI are reported. This process was repeated with each model implementation using a different subsurface feature as the mock surgical clip. On average, r=15 mm ROIs included 1 ± 1 targets, and r=30 mm ROIs included 4 ± 2 targets. At r=∞, the number of included data points is 21 ± 3, i.e. all subsurface points are targets expect for the feature included in the optimization. Evaluating with a small radius (r=15 mm) limits the coverage of evaluation, discarding points with no nearby subsurface data since these more isolated features are outside the scope of what would be realistic in the clinic. If a localization marker were more than 10 mm away from the target lesion, an additional marker would be placed closer to the target.

Though both the nearest neighbor and ROI approaches include one subsurface feature in each model optimization, they provide complimentary components of analysis. The nearest neighbor approach guarantees each subsurface feature is treated as an evaluation target exactly once. On the other hand, the ROI approach guarantees each subsurface feature is treated as an acquired data point included in the optimization function. The ROI approach, however, does not guarantee that every subsurface target is evaluated. As an example of this, if a subsurface feature is more than 15 mm away from all other targets, it will not be within any set of evaluation data at r=15 mm. The number of ROIs (i.e. number of model optimizations) evaluated for each subject is reported.

III. Results

A. Minimal Data-Driven Optimization

Mean registration errors were compared with paired t-tests (α=0.05). When compared to point based rigid registration, the nonrigid deformation correction without subsurface feature drivers offers significant improvement in fiducial registration error (FRE) and target registration error (TRE) (p<0.001), from FRE of 7.9 ± 1.6 to 2.4 ± 1.3 and TRE of 10.4 ± 2.3 mm to 6.3 ± 1.4 mm (Table I and Table II). Precomputing the modes of deformation takes, on average 13 ± 4 minutes using 64 processors on a 2.20 Ghz Intel® Xenon® CPU. The deformable correction takes, on average, 21 ± 18 seconds (median 14 s) for optimization on a single thread of a 2.20 Ghz Intel® Xenon® CPU. Additionally, for each method the model improvement over rigid registration is reported as

$$\frac{(error_{rigid}-error_{nonrigid})}{error_{rigid}} \times 100\%. \tag{4}$$

TABLE I
SUBSURFACE TARGET REGISTRATION ERROR (TRE),
MEAN ± STANDARD DEVIATION (MAXIMUM) IN MILLIMETERS

Case	Breast Volume (cm³)	Point Based Rigid Registration	Nonrigid Registration TRE	
			Nearest Neighbor	
			k=0	k=1
a	1228	9.1 ± 2.8 (15.0)	6.2 ± 2.4 (10.7)	4.0 ± 2.0 (8.8)
b	692	11.3 ± 4.1 (19.5)	6.1 ± 3.4 (13.1)	3.8 ± 1.6 (6.8)
c	663	9.7 ± 3.6 (21.0)	6.1 ± 3.3 (12.6)	3.8 ± 1.8 (8.1)
d	638	11.4 ± 7.2 (24.5)	7.4 ± 4.0 (15.3)	4.3 ± 2.0 (9.2)
e	614	10.8 ± 3.3 (15.9)	7.2 ± 2.7 (13.3)	5.2 ± 2.5 (9.9)
f	588	14.0 ± 3.8 (19.0)	7.5 ± 2.7 (12.1)	5.7 ± 2.5 (10.2)
g	398	6.5 ± 4.1 (14.2)	3.5 ± 1.9 (8.0)	2.5 ± 0.9 (4.4)
Mean	689	10.4 ± 2.3	6.3 ± 1.4	4.2 ± 1.0
Improvement over rigid registration			39%	60%

TABLE II
SURFACE FIDUCIAL REGISTRATION ERROR (FRE),
MEAN ± STANDARD DEVIATION (MAXIMUM) IN MILLIMETERS

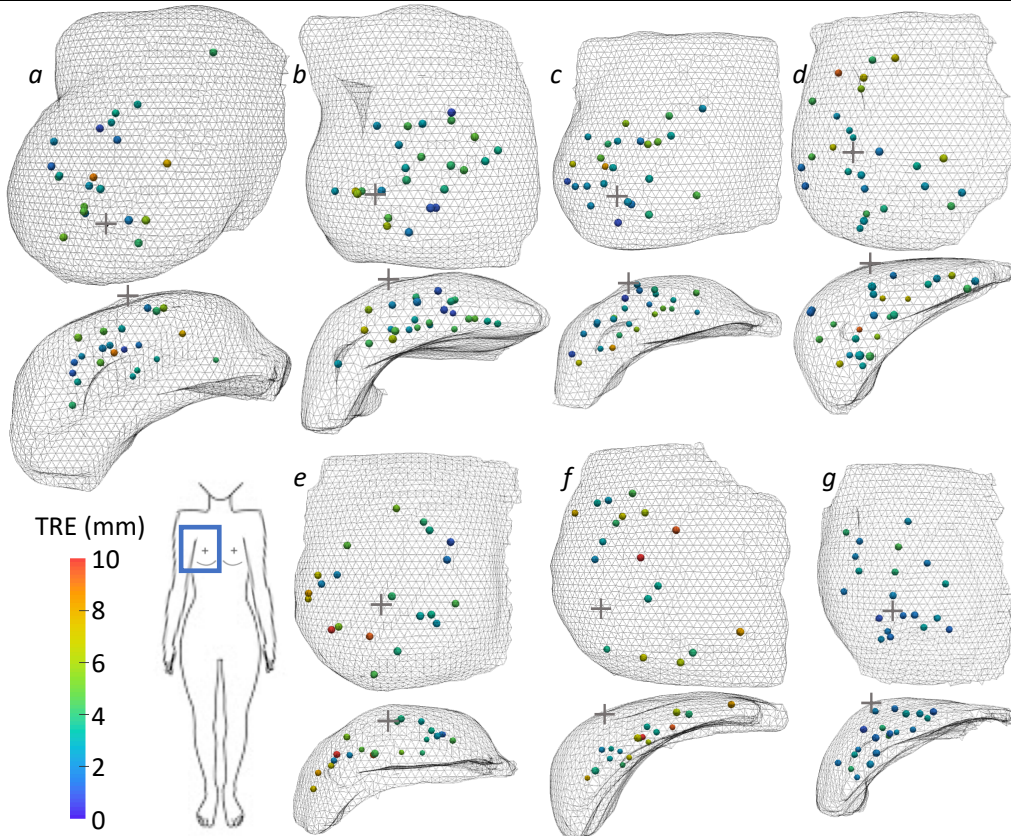| Case	Point Based Rigid Registration	Nonrigid Registration FRE	
		Nearest Neighbor	
		k=0	k=1
a	9.3 ± 2.8 (13.6)	5.1 ± 2.4 (10.7)	6.0 ± 2.5 (12.8)
b	9.6 ± 3.2 (17.3)	1.9 ± 0.9 (4.0)	2.9 ± 1.5 (8.5)
c	6.9 ± 2.2 (11.4)	2.6 ± 1.2 (5.4)	3.7 ± 1.7 (9.3)
d	6.3 ± 2.5 (14.4)	1.8 ± 0.9 (3.7)	2.4 ± 1.2 (8.1)
e	9.0 ± 4.4 (24.6)	2.3 ± 1.2 (6.6)	3.4 ± 1.7 (12.4)
f	8.3 ± 3.0 (13.6)	2.1 ± 1.3 (4.8)	2.9 ± 1.5 (7.7)
g	5.5 ± 1.7 (9.5)	1.2 ± 1.0 (4.7)	1.8 ± 1.1 (6.3)
Mean	7.9 ± 1.6	2.4 ± 1.3	3.6 ± 1.5
Improvement over rigid registration		69%	54%

Fig. 3. Distribution of subsurface target registration error (mm) with the k=1 nearest neighbor subsurface feature included as model input for each target evaluation. For each case the target locations are shown in the preoperative, or arm down, breast mesh from the anterior view (top) and inferior view (bottom). The subject's orientation is on the full-body diagram at the bottom left, with the blue box showing the approximate anterior field of view. The nipple is consistently marked +.
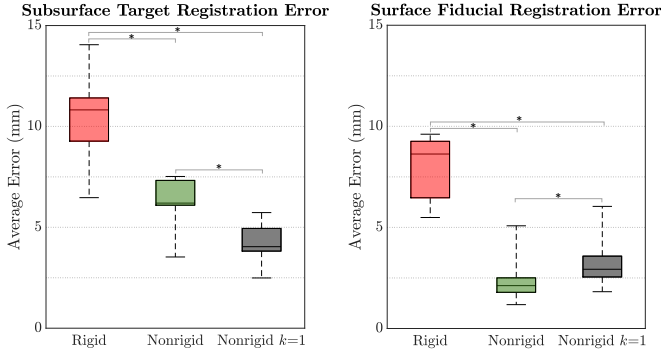
Fig. 4. Comparison of registration error (mm) for point based rigid versus nonrigid registration with varied amounts of subsurface features, where $k=1$ indicates that a neighboring subsurface feature is included in the model optimization. Significant differences exceeding $p<0.001$ are reported with *.

B. Inclusion of a Single Nearest Neighbor Subsurface Feature

The TRE significantly improves with the addition of subsurface feature data from $k=0$ to $k=1$ ($p<0.001$). Conversely, the FRE significantly worsens with the inclusion of a subsurface feature point from $k=0$ to $k=1$ ($p<0.001$). Subsurface TREs are presented in Table I, and residual surface FREs are presented in Table II. Spatial distribution of subsurface target error with the inclusion of the nearest neighbor subsurface point ($k=1$) is visualized in Figure 3. This figure shows both the broad distribution of targets, as well as the distances between targets and their nearest neighbors. Left breasts are reflected so each breast mesh is in the same anatomical orientation, with the arm on the left and the sternum on the right of the image, as indicated on the full-body diagram. Breast volumes are also reported in Table I. While the model performs best in the smallest breast volume, for this dataset there is no observable trend with respect to volumes. Figure 4 shows the distribution of average error across the seven cases, and statistical comparisons. For all registration methods reported in Figure 4, each target is evaluated exactly once.

C. Accuracy in Regions of Interest

When evaluation was limited to a region of interest ($r=30$ mm), registration error significantly decreased in comparison to evaluation across the whole breast with $r=\infty$ ($p<0.001$). As

the radius decreases, the TRE continues to significantly improve from $r=30$ mm to $r=15$ mm ($p=0.001$). For $r=\infty$, the addition of one subsurface clip resulted in higher error when compared to TRE for the model run with no subsurface clip ($p=0.026$). In other words, although local target errors improve, far field errors worsen.

Results for regions of interest with decreasing radii are presented in Table III and distribution of average target error is shown in Figure 5. As previously discussed, as the radius decreases, some clips no longer have targets within the region of interest and are therefore not included in evaluation. This behavior is reflected in the number of ROIs, also presented in Table III. Though the average number of regions evaluated remains constant from $r=\infty$ mm to $r=30$ mm, the average TRE drops significantly, reflecting higher accuracy in a region of interest, even when model accuracy is evaluated across a wide spatial distribution of regions. While the average TRE improves significantly again when the radius is reduced to $r=15$ mm, the number of evaluated regions drops down to 14 ± 5. This reduction in the number of regions evaluated means that our analysis is limited to the more central regions of the breast where subsurface features are more densely distributed. The density of subsurface points can be observed in Figure 3.
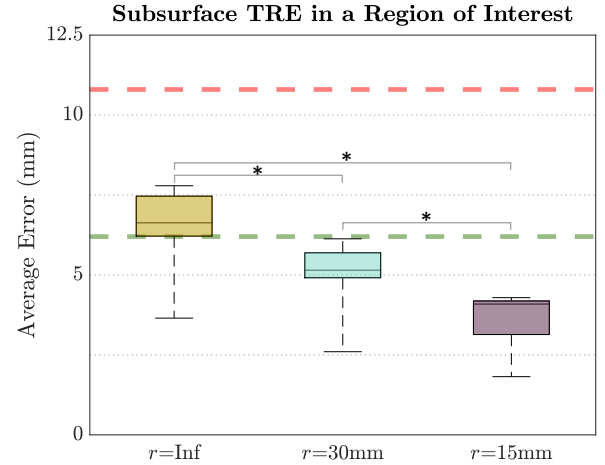

Fig. 5. Comparison of subsurface target registration error (TRE) in millimeters, varying the radius of the region of interest, r, centered on a subsurface clip included in driving the model. Dashed lines represent median TRE for rigid (red) and nonrigid (green) registration with no subsurface clips included. Significant differences exceeding $p\leq0.001$ are reported with *.

TABLE III
SUBSURFACE TARGET REGISTRATION ERROR (TRE)
FOR NONRIGID CORRECTION IN A REGION OF INTEREST (ROI) WITH RADIUS r AROUND 1 CLIP
MEAN ± STANDARD DEVIATION (MAXIMUM) IN MILLIMETERS

Case	$r = \infty$ mm		$r = 30$ mm		$r = 15$ mm	
	Avg ± std (Max)	# of ROIs	Avg ± std (Max)	# of ROIs	Avg ± std (Max)	# of ROIs
a	6.6 ± 2.4 (12.7)	22	5.3 ± 2.3 (10.9)	21	4.1 ± 2.1 (8.8)	15
b	6.3 ± 3.1 (13.7)	25	5.0 ± 2.2 (10.6)	25	4.3 ± 1.9 (7.7)	21
c	6.2 ± 2.8 (13.4)	25	4.9 ± 2.8 (10.7)	24	3.9 ± 1.6 (6.7)	14
d	7.8 ± 3.7 (17.6)	26	5.8 ± 2.4 (11.3)	26	2.9 ± 0.9 (4.3)	17
e	7.2 ± 2.8 (14.0)	21	5.8 ± 2.8 (12.5)	20	4.2 ± 2.0 (8.0)	13
f	7.6 ± 2.7 (13.4)	18	6.1 ± 2.6 (11.4)	17	4.1 ± 1.6 (6.8)	8
g	3.7 ± 1.8 (8.3)	20	2.6 ± 1.1 (5.8)	20	1.8 ± 0.7 (3.0)	8
Mean	6.5 ± 1.4	22	5.0 ± 1.1	22	3.6 ± 0.9	14
Improvement	38%		52%		65%	

IV.   Discussion

The method presented here demonstrates state-of-the art localization in seven human breasts, with comprehensive target sampling in varying volumes. The method offers consistent, significant improvement with 50–60% correction over conventional rigid registration. This algorithm provides subsurface target errors consistently on the order of 1 cm or less in targets well distributed throughout seven breast volumes undergoing mock preoperative-to-surgical deformations. This modeling framework can correct for nonrigid deformations fast enough to provide accurate guidance at patient bedside. The presented method outperforms previous findings with less variability.

This model correction technique combined with sparse intraprocedural data can be used to reconstruct computational images of the deformed anatomy for use in intraoperative guidance. An example of deformed computational images is shown in Figure 6 for case *d*. Qualitatively, the subsurface feature alignment improves significantly, along with the alignment of the skin surface and chest wall, displayed as grey contours in all panels. The feature indicated by the black arrow is not aligned for rigid registration (red) but becomes aligned when the nonrigid correction methods are employed (green and yellow). It should be noted that the feature indicated by the white arrow appears to be potentially aligned with rigid registration (red). However, in further multi-slice examination, there is still significant misalignment in the inferior/superior direction that cannot be visualized in this 2D example. With careful observation, there is a noticeable shape discrepancy and this is a result of the rigidly aligned feature being located several image slices inferior to the true feature location. Similarly, the nonrigid correction with no subsurface feature points included ($k=0$, green) is notably misaligned in the medial-lateral (left-right) direction near the white arrow; however, the two nonrigidly corrected images more closely predict the true shape of that feature and better align that feature in the inferior/superior direction. Finally, observing the same structure with the nearest subsurface neighbor ($k=1$) included as additional data, the reconstructed computational image shows excellent agreement in location and shape (yellow). It is also important to note that the included subsurface data point was ~10 mm from the feature of interest designated by the white arrow. Whereas the far-field accuracy is slightly compromised at the surface above the well-fit features, the $k=1$ approach improves alignment for the feature further away (designated by the black arrow) at approximately ~30 mm away. It is this regional accuracy that is most clinically relevant within the context of margin management. Though even without the use of an additional subsurface feature, the $k=0$ approach (green) still shows significant improvement over conventional rigid registration (red).

Model accuracy is clinically relevant across the whole volume but demonstrates even higher fidelity in a region of interest around subsurface data. Results using the proposed method suggest that localization error of the tumor boundary is achievable to less than 4 mm on average within a 15 mm radius of a biopsy clip, and to 5 mm on average within a 30
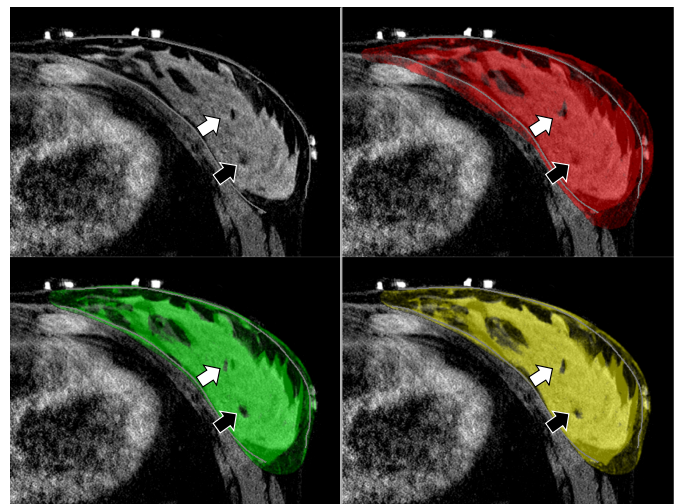

Fig. 6. An axial slice of registered computational images overlaid on the ground truth image in the fully abducted arm position for case d. In all panels, segmentations of the chest wall and skin surface are outlined in gray. The rigidly registered image is shown in red. The model deformed image computed without subsurface features ($k=0$) is shown in green. In yellow is the model deformed image computed with one additional subsurface point ($k=1$) approximately 10 mm from the feature indicated by the white arrow.

mm radius. In the context of breast lesion sizes as discussed in Section II.F with the planned margin of healthy tissue included, the large majority of patients would have resection volumes smaller than the regions of interest discussed here. Intraoperative localization accuracy for over 75% of patients can be expected to be on the order of 5 mm. For patients with smaller lesions – still over 50% of patients – accuracy of a guidance system using this method could be expected to be less than 4 mm on average [37, 38].

Previous works evaluated performance solely based on tumor overlap metrics, limiting error analysis to one region of interest around the tumor. While tumor overlap is valuable for evaluating final oncological margins, it is incomplete for evaluating the general accuracy of a localization strategy. Point-based measurements instead provide precise accuracy measurements that are not subject to the ambiguities associated with surface or volume alignments. Additionally, because the full volumetric data provided many subsurface points, the analysis here was extended to include at least 8 regions of interest in each breast volume. Though the proposed method remains to be evaluated in patients, local accuracy is reported in many regions of interest, and full-field accuracy is quantified across well-sampled precise points.

Limitations of this study largely fall into the following categories: the use of full volumetric data from supine MR images, model assumptions, limited population, and the shift to existing standard of care. First, while the use of full volumetric data provides realistic extent and thorough validation targets, it does come with limitations. Although clinically acquired intraoperative data would likely provide fewer evaluation targets, true intraoperative measurement sources may include additional noise or localization errors. Tracked ultrasound measurements with probe deformation correction have reported localization accuracy on the order of 3 mm in vivo [40], and electromagnetically tracked seeds have

reported accuracies below 1 mm, though accuracy degrades with distance [41]. In the mock intraoperative setup in [8], reproducibility of surface fiducials manually designated with a stylus was measured to be 1.5 ± 0.1 mm (case *d* here). While these localization errors are not considered in this work, segmentation error may add similar noise and impact the results. In that same instrumentation analysis in [8], reproducibility of surface point picking in supine MR images was measured as 1.6 ± 0.4 mm, though this quantification cannot be directly translated to the localization error of subsurface points. Related to the use of MR data in this study, other limiting factors include image quality, segmentation error, and spatial distribution of validation targets. Many cases had few or no distinct features in the medial breast tissue as visible in Figure 3. Fortunately, this area of the breast experiences smaller displacements, and the bulk of breast shift occurs farther from the sternum [8].

Second, in this model, precomputed modes of deformation are generated based on isotropic, homogeneous, and linear elastic assumptions. The results may be improved with a model that incorporates anisotropy, heterogeneity, co-rotational or nonlinear elasticity, body forces, or a different distribution of boundary conditions. Though breast tissue is often considered hyperelastic, the linear elastic assumption here allows modes of deformation to be quickly scaled and combined for improved intraoperative localization. Despite this reduction in complexity, the model performance still significantly improves upon conventional registration and the approach using superposition of these linear modes makes model predictions fast enough to be feasible in the operating room. While outside the scope here, it would be interesting to compare performance with a superposition of hyperelastic modes, though a non-linear combination of these modes would be complex and a linear combination of these modes would alter some hyperelastic behavior. Similarly, accounting for local rigid body motion with techniques such as co-rotational finite elements may improve results further [42]. Constitutive models and large deformations are important considerations but their election must also be influenced by other considerations (e.g. computational speed, anisotropy, anatomical structures – Cooper's ligaments, glandular tissue milk perfusion, etc.)

Another limitation of current assumptions is that this registration approach is not well suited to account for volume changes, though breast volume varies with the menstrual cycle [43, 44]. Depending on the time between imaging and surgery, preoperative and intraoperative breast volumes may differ. While, the majority of breast cancer patients are postmenopausal [45], if hormonal changes in breast volume are later determined to be paramount within an image guidance framework, additional deformation modes could be considered to allow for volume changes without additional strain energy penalty as suggested in [46]. Alternatively, supine MR imaging could feasibly be conducted on the same day to minimize volume change effects. The suggested or allowable time between preoperative imaging and surgery remains to be investigated.

Though the current the implementation does not consider intraoperative deformations due to incisions, future work should incorporate modes to model resection. Interestingly, there are some initial efforts toward this that also use deformation modes in the context of tissue retraction [47]. However, in related work, even a rigid registration framework at surgical onset was able to obtain reoperation rates lower than wire-guided localization (9% and 19% respectively) [19]. The work presented here shows a significant improvement beyond the accuracy of rigid registration, suggesting that a nonrigid correction framework could provide the accuracy required to push the field beyond the current 10-20% reoperation rates.

Similarly, model performance was not investigated with varied levels of input data sparsity. Effects of denser sparse data density and extent, especially along the chest wall, remain to be studied more completely. Though it should be noted, in results not presented here, deformable correction was also evaluated using only the breast surface fiducials and skin surface. In these surface-driven corrections, the surface points are allowed to fit more closely at the expense of unpenalized subsurface structural misalignment. When compared to rigid registration, surface-driven correction still significantly improves FRE and TRE (p<0.001) with FRE of 2.2 ± 1.3 mm providing 72% improvement, and TRE of 6.6 ± 1.5 mm providing 39% improvement. When compared to deformable correction with surface and chest wall information (i.e. compared to model correction results reported in Section III.A with k=0) surface-driven correction improves FRE (p=0.006) and worsens TRE (p=0.049). Though these results demonstrate that model correction is valuable with surface data alone, more data and analyses are required to fully investigate the importance of intraoperative measurements of the chest wall position.

The effect of more limited surface data also remains to be evaluated. Feasibility of collecting the full breast surface has been demonstrated by several groups [18-20], but a stationary camera as in [48] is more practical for re-collecting surfaces without interfering with workflow to provide continued alignment beyond an initial registration. Surfaces collected with stationary cameras are often limited by line-of-sight constraints, especially for larger breast volumes. The effect of these line-of-sight constraints on data collection are not considered here, but should be investigated in future works. If necessary, tracked instruments could be used to collect intraoperative data to augment a camera-acquired surface.

Third, the population of subjects included in this study is limited; the average age of volunteers in this study was 29 years, and there are only seven subjects. The majority of breast cancer patients are between 50 and 70 years of age [49], and only one of the healthy volunteers here is in that age range, at 57 years. As tissue properties are known to vary with age and menopausal status, future works may investigate correction accuracy on breast cancer patients. With respect to the number of subjects, this limited sample size was sufficient for strongly powered statistical tests indicating nonrigid registration improves beyond rigid registration, and that the

inclusion of one subsurface point improves prediction accuracy even further. Future work could include correction accuracy across a wider range of ages and breast volumes.

Lastly, there are a few considerations within the context of the existing standard of care for breast cancer. Though the proposed method necessitates supine MR imaging, it is not currently standard of care. However, in a recent study comparing diagnostic value of contrast-enhanced breast MR in 120 patients with lesions undergoing both prone and supine imaging, interestingly there was no difference in image quality between prone and supine positions for both image resolution and diagnostic value [50]. The only difference was in geometric lesion extension which was to be expected given the change in loading conditions. Studies like the one presented here offer a rationale for changing diagnostic protocols for surgical candidates in the future. In addition, a paradigm shift that improves localization would likely result in improved patient outcomes and reduced costs associated with reoperations. Furthermore, if one could generate localizable biopsy clips, it would take full advantage of our findings regarding the impact of subsurface data. It would also have the benefit of eliminating the painful device placement procedures for seed-based methods used by many hospitals, and reduce the growing burden placed on radiology departments.

V. Conclusion

Existing image-guided breast surgery investigations have largely employed conventional image-guided surgery techniques that used rigid registration. These early investigations reflect accuracy and margin management similar to that of seed-based methods [19]. While anecdotal results using nonrigid approaches and sparse data have been promising [18, 28], the work herein is the first to significantly demonstrate the potential for better margin management by accounting for volumetric nonrigid deformations. When compared to conventional rigid registration, the method consistently provides significantly improved registration accuracy across all subjects. Furthermore, including just one nearby subsurface feature significantly improves registration accuracy even further and opens the possibility of integrating the capability with seed-based methods or similar alternatives. Another important strength of the work is that the approach is driven with realistic sparse mock-intraoperative data, and the registrations can be produced at clinically feasible speeds. While advancements are still needed, the proposed approach is robust, accurate, and compatible with surgical workflows such that it is quite reasonable to see this framework becoming a surgical technology as ubiquitous as image guidance has already become within neurosurgical standard of care.

References

[1]   U. Ayachit, *The paraview guide: a parallel visualization application*. Kitware, Inc., 2015.

[2]   R. L. Siegel, K. D. Miller, H. E. Fuchs, and A. Jemal, "Cancer statistics, 2022," *CA: a cancer journal for clinicians,* 2022.

[3]   M. Golshan *et al.*, "Impact of neoadjuvant chemotherapy in stage II–III triple negative breast cancer on eligibility for breast-conserving surgery and breast conservation rates: surgical results from CALGB 40603 (Alliance)," *Annals of surgery,* vol. 262, no. 3, p. 434, 2015.

[4]   E. Guadagnoli, J. C. Weeks, C. L. Shapiro, J. H. Gurwitz, C. Borbas, and S. B. Soumerai, "Use of breast-conserving surgery for treatment of stage I and stage II breast cancer," *Journal of Clinical Oncology,* vol. 16, no. 1, pp. 101-106, 1998.

[5]   L. A. Carbonaro, P. Tannaphai, R. M. Trimboli, N. Verardi, M. P. Fedeli, and F. Sardanelli, "Contrast enhanced breast MRI: spatial displacement from prone to supine patient's position. Preliminary results," *European journal of radiology,* vol. 81, no. 6, pp. e771-e774, 2012.

[6]   B. K. Byrd *et al.*, "The shape of breast cancer," *Breast Cancer Research and Treatment,* pp. 1-8, 2020.

[7]   M. A. Mallory *et al.*, "Feasibility of Intraoperative Breast MRI and the Role of Prone Versus Supine Positioning in Surgical Planning for Breast-Conserving Surgery," *The Breast Journal,* vol. 23, no. 6, pp. 713-717, Nov 2017.

[8]   W. L. Richey, J. S. Heiselman, M. Luo, I. M. Meszoely, and M. I. Miga, "Impact of deformation on a supine-positioned image guided breast surgery approach," *International Journal of Computer Assisted Radiology and Surgery,* Journal vol. 16, no. 11, p. 2055—2066, 2021.

[9]   M. L. Marinovich, N. Noguchi, M. Morrow, and N. Houssami, "Changes in reoperation after publication of consensus guidelines on margins for breast-conserving surgery: a systematic review and meta-analysis," *JAMA surgery,* vol. 155, no. 10, pp. e203025-e203025, 2020.

[10]   L. Havel, H. Naik, L. Ramirez, M. Morrow, and J. Landercasper, "Impact of the SSO-ASTRO margin guideline on rates of re-excision after lumpectomy for breast cancer: a meta-analysis," *Annals of surgical oncology,* vol. 26, no. 5, pp. 1238-1244, 2019.

[11]   S. G. B. de Koning, M.-J. T. V. Peeters, K. Jóźwiak, P. A. Bhairosing, and T. J. Ruers, "Tumor resection margin definitions in breast-conserving surgery: systematic review and meta-analysis of the current literature," *Clinical breast cancer,* vol. 18, no. 4, pp. e595-e600, 2018.

[12]   M. Morrow *et al.*, "Trends in reoperation after initial lumpectomy for breast cancer: addressing overtreatment in surgical management," *JAMA oncology,* vol. 3, no. 10, pp. 1352-1357, 2017.

[13]   A. Monaghan, N. Chapinal, L. Hughes, and C. Baliski, "Impact of SSO-ASTRO margin guidelines on reoperation rates following breast-conserving surgery," *The American Journal of Surgery,* vol. 217, no. 5, pp. 862-867, 2019.

[14]   G. K. Cakmak, A. U. Emre, B. Bahadir, O. Tascilar, and S. Ozkan, "Surgeon performed continuous intraoperative ultrasound guidance decreases re-excisions and mastectomy rates in breast cancer," (in English), *Breast,* Article vol. 33, pp. 23-28, Jun 2017.

[15]   H. Eggemann, T. Ignatov, S. D. Costa, and A. Ignatov, "Accuracy of ultrasound-guided breast-conserving surgery in the determination of adequate surgical margins," *Breast Cancer Research and Treatment,* vol. 145, no. 1, pp. 129-136, 2014.

[16]   M. W. Barentsz *et al.*, "Intraoperative ultrasound guidance for excision of non-palpable invasive breast cancer: a hospital-based series and an overview of the literature," (in English), *Breast Cancer Research and Treatment,* Article vol. 135, no. 1, pp. 209-219, Aug 2012.

[17]   V. S. Klimberg, "Advances in the diagnosis and excision of breast cancer," *The American Surgeon,* vol. 69, no. 1, p. 11, 2003.

[18]   R. H. Conley *et al.*, "Realization of a biomechanical model-assisted image guidance system for breast cancer surgery using supine MRI," (in English), *International Journal of Computer Assisted Radiology and Surgery,* Article vol. 10, no. 12, pp. 1985-1996, Dec 2015.

[19]   R. J. Barth *et al.*, "A Randomized Prospective Trial of Supine MRI-Guided Versus Wire-Localized Lumpectomy for Breast Cancer," *Annals of Surgical Oncology,* pp. 1-10, 2019.

[20]   S. L. Perkins, M. A. Lin, S. Srinivasan, A. J. Wheeler, B. A. Hargreaves, and B. L. Daniel, "A mixed-reality system for breast surgical planning," in *2017 IEEE International Symposium on*

Mixed and Augmented Reality (ISMAR-Adjunct), 2017, pp. 269-274: IEEE.

[21] P. Siegler, C. M. Holloway, P. Causer, G. Thevathasan, and D. B. Plewes, "Supine breast MRI," *J Magn Reson Imaging,* vol. 34, no. 5, pp. 1212-7, Nov 2011.

[22] R. M. Mann, C. K. Kuhl, and L. Moy, "Contrast-enhanced MRI for breast cancer screening," *Journal of Magnetic Resonance Imaging,* vol. 50, no. 2, pp. 377-390, 2019.

[23] E. C. Gombos *et al.*, "Intraoperative supine breast MR imaging to quantify tumor deformation and detection of residual breast cancer: preliminary results," *Radiology,* vol. 281, no. 3, pp. 720-729, 2016.

[24] S. Joukainen *et al.*, "Feasibility of mapping breast cancer with supine breast MRI in patients scheduled for oncoplastic surgery," *European Radiology,* Journal Article vol. 29, no. 3, pp. 1435-1443, August 17 2019.

[25] M. Sakakibara *et al.*, "Breast-Conserving Surgery Using Projection and Reproduction Techniques of Surgical-Position Breast MRI in Patients with Ductal Carcinoma In Situ of the Breast," *Journal of the American College of Surgeons,* vol. 207, no. 1, pp. 62-68, 2008/07/01/ 2008.

[26] Z.-Y. Wu *et al.*, "Breast-conserving surgery with 3D-printed surgical guide: a single-center, prospective clinical study," *Scientific Reports,* vol. 11, no. 1, pp. 1-8, 2021.

[27] M. J. Pallone, S. P. Poplack, H. B. Avutu, K. D. Paulsen, and R. J. Barth, Jr., "Supine breast MRI and 3D optical scanning: a novel approach to improve tumor localization for breast conserving surgery," *Annals of Surgical Oncology,* vol. 21, no. 7, pp. 2203-8, Jul 2014.

[28] M. Ebrahimi, P. Siegler, A. Modhafar, C. M. Holloway, D. B. Plewes, and A. L. Martel, "Using surface markers for MRI guided breast conserving surgery: a feasibility survey," *Phys Med Biol,* vol. 59, no. 7, pp. 1589-605, Apr 7 2014.

[29] J. S. Heiselman, W. R. Jarnagin, and M. I. Miga, "Intraoperative correction of liver deformation using sparse surface and vascular features via linearized iterative boundary reconstruction," *IEEE Transactions on Medical Imaging,* vol. 39, no. 6, pp. 2223-2234, 2020.

[30] P. A. Yushkevich *et al.*, "User-guided 3D active contour segmentation of anatomical structures: significantly improved efficiency and reliability," *Neuroimage,* vol. 31, no. 3, pp. 1116-1128, 2006.

[31] J. M. Sullivan Jr, G. Charron, and K. D. Paulsen, "A three-dimensional mesh generator for arbitrary multiple material domains," *Finite Elements in Analysis and Design,* vol. 25, no. 3-4, pp. 219-241, 1997.

[32] S. S. Antman, D. Carlson, G. Fichera, M. Gurtin, and P. Naghdi, C. Truesdell, Ed. *Mechanics of Solids: Volume II: Linear Theories of Elasticity and Thermoelasticity, Linear and Nonlinear Theories of Rods, Plates, and Shells*. Springer, 1972, p. 755.

[33] D. R. Lynch, *Numerical partial differential equations for environmental scientists and engineers: a first practical course*. Springer Science & Business Media, 2004.

[34] T. S. Pheiffer, R. C. Thompson, D. C. Rucker, A. L. Simpson, and M. I. Miga, "Model-based correction of tissue compression for tracked ultrasound in soft tissue image-guided surgery," *Ultrasound in Medicine and Biology,* vol. 40, no. 4, pp. 788-803, 2014.

[35] N. Janssen *et al.*, "Real-time wireless tumor tracking during breast conserving surgery," *International journal of computer assisted radiology and surgery,* vol. 13, no. 4, pp. 531-539, 2018.

[36] (2021, July 27, 2021). *SmartClip™ Soft Tissue Marker*. Available: https://elucentmedical.com/

[37] R. F. Brem, J. W. Hoffmeister, G. Zisman, M. P. DeSimio, and S. K. Rogers, "A computer-aided detection system for the evaluation of breast cancer by mammographic appearance and lesion size," *American Journal of Roentgenology,* vol. 184, no. 3, pp. 893-896, 2005.

[38] L. Liberman, G. Mason, E. A. Morris, and D. D. Dershaw, "Does size matter? Positive predictive value of MRI-detected breast lesions as a function of lesion size," *American Journal of Roentgenology,* vol. 186, no. 2, pp. 426-430, 2006.

[39] N. Krekel *et al.*, "Excessive resections in breast-conserving surgery: a retrospective multicentre study," *The breast journal,* vol. 17, no. 6, pp. 602-609, 2011.

[40] T. S. Pheiffer and M. I. Miga, "Toward a generic real-time compression correction framework for tracked ultrasound," *International journal of computer assisted radiology and surgery,* vol. 10, no. 11, pp. 1777-1792, 2015.

[41] A. M. Franz, T. Haidegger, W. Birkfellner, K. Cleary, T. M. Peters, and L. Maier-Hein, "Electromagnetic tracking in medicine—a review of technology, validation, and applications," *IEEE transactions on medical imaging,* vol. 33, no. 8, pp. 1702-1725, 2014.

[42] J. Georgii and R. Westermann, "Corotated Finite Elements Made Fast and Stable," *VRIPHYS,* vol. 8, pp. 11-19, 2008.

[43] Z. Hussain, N. Roberts, G. Whitehouse, M. Garcia-Finana, and D. Percy, "Estimation of breast volume and its variation during the menstrual cycle using MRI and stereology," *The British journal of radiology,* vol. 72, no. 855, pp. 236-245, 1999.

[44] D. Milligan, J. Drife, and R. Short, "Changes in breast volume during normal menstrual cycle and after oral contraceptives," *Br Med J,* vol. 4, no. 5995, pp. 494-496, 1975.

[45] R. Ghiasvand, H.-O. Adami, I. Harirchi, R. Akrami, and K. Zendehdel, "Higher incidence of premenopausal breast cancer in less developed countries; myth or truth?," *BMC cancer,* vol. 14, no. 1, pp. 1-8, 2014.

[46] J. S. Heiselman, "Mechanics-based estimation of intraoperative soft tissue deformation for enhancing navigation during image-guided liver intervention," Vanderbilt University, 2020.

[47] I. Chen, R. E. Ong, A. L. Simpson, K. Sun, R. C. Thompson, and M. I. Miga, "Integrating retraction modeling into an atlas-based framework for brain shift prediction," *IEEE Transactions on Biomedical Engineering,* vol. 60, no. 12, pp. 3494-3504, 2013.

[48] W. L. Richey, J. Heiselman, M. Luo, I. M. Meszoely, and M. I. Miga, "Textual fiducial detection in breast conserving surgery for a near-real time image guidance system," in *Medical Imaging 2020: Image-Guided Procedures, Robotic Interventions, and Modeling*, 2020, vol. 11315, p. 113151L: International Society for Optics and Photonics.

[49] C. E. DeSantis *et al.*, "Breast cancer statistics, 2019," *CA: A Cancer Journal for Clinicians,* vol. 69, no. 6, pp. 438-451, 2019.

[50] A. Fausto *et al.*, "Feasibility, Image Quality and Clinical Evaluation of Contrast-Enhanced Breast MRI Performed in a Supine Position Compared to the Standard Prone Position," *Cancers,* vol. 12, no. 9, p. 2364, 2020.